International Journal of Solids and Structures 51 (2014) 4406–4413

Contents lists available at ScienceDirect

International Journal of Solids and Structures

journal homepage: www.elsevier.com/locate/ijsolstr

Modeling finite thickness slab perforation using a coupled Eulerian–Lagrangian approach

Jesse A. Sherburn *, Michael I. Hammons, Michael J. Roth

U.S. Army Engineer Research and Development Center, Vicksburg, MS, USA

ARTICLE INFO

Article history:
Received 29 January 2014
Received in revised form 7 August 2014
Available online 4 October 2014

Keywords:
Penetration
Coupled Eulerian–Lagrangian method
Concrete
Constitutive law
Stochastic

ABSTRACT

A coupled Eulerian–Lagrangian (CEL) method can be used to model many types of dynamic events. Projectile penetration through solids is particularly well-suited to a CEL method. In this study the CEL method in the commercially-available code Abaqus was used to model a near rigid projectile perforating finite thickness concrete slabs. A near rigid projectile can be modeled as a Lagrangian material with distinct material interfaces, while the solid target can be modeled as an Eulerian material capable of large deformations. An improved concrete constitutive model is also described that was implemented into Abaqus as a user material model. A simplified stochastic model was also implemented to capture some of the heterogeneous nature of concrete. The CEL simulations are compared to experimental data to demonstrate the utility of this method for this type of perforation event.

Published by Elsevier Ltd.

1. Introduction

Penetration of a projectile into soil, rock or concrete is a problem of interest to the military and civil communities. Methods to predict penetration into brittle materials have seen significant developments since World War II, with much effort focused on synthesis of empirical data with analytical tools (White, 1946; Kennedy, 1976; Backman and Goldsmith, 1978; Wilkins, 1978; Jonas and Zukas, 1978; Aptukov, 1990; Ben-Dor et al., 2005).

Modern computational capabilities have spurred increased interest in numerical first-principles approaches to penetration calculations in concrete targets. Most computational approaches have focused on either Lagrangian finite element (FE) or Eulerian finite difference (FD) methods (Anderson, 1987). One advantage of the Lagrangian FE method is that the interface between the penetrator and the target is well defined and readily tracked. Behavior at material contact interfaces is enforced through spatial slide surfaces, which must be defined *a priori*. A disadvantage of this method is that severe distortion of the mesh in high-velocity impact problems causes computational difficulties resulting in very small time steps and numerical errors. Rezoning the mesh in areas of high distortion has been used to overcome these problems. However, the rezoning process must often be repeated many times resulting in considerable computational overhead (Brown et al., 2002). Other techniques like element erosion (Belytschko and Lin, 1987; Johnson and Stryk, 1987; Sewell et al., 1990) have also been proposed to overcome the problem of mesh distortion in these high-velocity impact problems. Recent advancements in Lagrangian meshfree methods for large deformation and fragmentation problems (Chen et al., 1996; Johnson et al., 1996, 2000; Guan et al., 2011) have provided new capabilities for penetration modeling due to their ability to model large distortion, material separation, and evolving contact conditions.

Eulerian FD methods accommodate large distortions readily, and no *a priori* definition of contact surfaces is required. However, the material interfaces are not distinct, and heuristics must be introduced to prevent the smearing of the boundary between the penetrator and target (Anderson, 1987).

A coupled Eulerian–Lagrangian (CEL) method provides a natural approach to a usable, general-purpose penetration model (Brown et al., 2002). The penetrator is modeled using a Lagrangian formulation, while the target is modeled using an Eulerian formulation. The Lagrangian domain moves through the Eulerian mesh, and heuristics are required to couple the responses of the two domains. The most common approach involves applying the Eulerian pressures to the Lagrangian mesh, and applying the Lagrangian nodal velocities as boundary conditions on the Eulerian mesh. The boundary of the Lagrangian domain is used to define the boundary between the penetrator and target. Conditions must be satisfied to ensure that the two materials do not occupy the same space at each time step (Benson, 1992).

* Corresponding author at: 3909 Halls Ferry Road, Vicksburg, MS 39180-6199, USA. Tel.: +1 601 634 3202.
E-mail address: jesse.a.sherburn@usace.army.mil (J.A. Sherburn).

http://dx.doi.org/10.1016/j.ijsolstr.2014.09.007
0020-7683/Published by Elsevier Ltd.

All numerical penetration model approaches for high velocity impacts in concrete require adoption of a brittle material constitutive law. The constitutive law must be able to predict the salient characteristics of the material response resulting from impact, penetration and perforation. Forrestal and Luk (1992) developed relationships to predict the penetration of ogive-nose projectiles into soils after normal impact based on a spherical cavity expansion model incorporating three stress-dependent constitutive models. However, Forrestal et al. (1994) recognized that penetration studies often lack the material characterization data required to properly calibrate these constitutive models. To this end, they proposed a semi-empirical method to predict the depth of impact in a concrete target that required only the unconfined compressive strength of the concrete and a dimensionless empirical constant that is used to modify the unconfined compressive strength and density of the concrete.

A number of models have been proposed and implemented in various codes. The material property data required for calibration of these constitutive models must be obtained from appropriate laboratory material characterization tests (Cargile, 1999). One of the most common constitutive laws used in both Lagrangian and Eulerian formulations was developed by Holmquist et al. (1993) and is commonly referred to as the Holmquist–Johnson–Cook (HJC) model. The model was formulated for large strains, high strain rates, and high pressure simulations. Material damage, rate effects, and crushing were accommodated as a function of the stress state and air void ratio.

In this paper, a CEL approach is used to model penetration and perforation of a brittle concrete target by a high-velocity, ogive-nose steel projectile. A constitutive model is adopted similar to the HJC model that also includes third-invariant dependency in the failure surface, which was shown to be important in perforation problems (Fossum and Brannon, 2006). For this study, a variation of the Advanced Fundamental Concrete (AFC) model (Adley et al., 2010) was used to model the concrete. The model will be discussed in the subsequent section.

The AFC model is discussed in Section 2 along with additional features included that were not implemented in the original version of AFC given in Adley et al. (2010). In Section 3 the experimental penetration problems, which were modeled by the CEL method, are described. The setup of the CEL simulations is discussed in Section 4. Section 5 discusses the simulation results, and Section 6 provides concluding remarks.

2. Material model

The AFC model, developed by the U.S. Army Engineer Research and Development Center, is a three-invariant plasticity model that includes hydrostatic crushing, material yielding, plastic flow, and damage effects. A material fit was produced for WES5000, a 38.2 MPa compressive strength concrete, by Adley et al. (2010) and was used in this study. In the AFC model the hydrostatic and deviatoric responses are assumed to be decoupled. The hydrostatic response is composed of three separate regions, as shown in Fig. 1. The first region (zone I in Fig. 1) is the low-pressure elastic portion that extends to the initial crushing pressure defined by two constants, C_6 and C_7, which are the initial crushing pressure and initial crushing volumetric strain, respectively. The second region (zone II in Fig. 1) is a nonlinear crushing region given by

$$P = K_1 + K_2\mu^2 + K_3\mu^3, \tag{1}$$

where K_1, K_2, and K_3 are material constants, and μ is volumetric strain. The third region (zone III in Fig. 1) describes the response of the fully crushed material. Once the volumetric strain reaches a predefined locking strain, C_9, the model assumes linear locking of fully crushed and compacted material defined by a locking bulk modulus, C_8. Upon unloading in the linear locking region, the response follows the locking bulk modulus, C_8. The compression failure surface is defined by

$$S_Y^{comp} = (C_1 - (C_2 + (C_1 - C_2)d)e^{A_n I_1} - C_4 I_1(1 + C_3 \ln(\dot{\varepsilon}_n)), \tag{2}$$

where C_1, C_2, C_3, C_4, and A_n are material constants and d, I_1, and $\dot{\varepsilon}_n$ are the damage, first stress invariant, and a normalized strain-rate, respectively. The strain-rate in Eq. (2) is normalized by the reference strain-rate of 0.0001 s^{-1}. Fig. 2 shows the compression failure surface for loading at both a quasistatic (0.001 s^{-1}) strain rate and a strain rate of 100 s^{-1}. Expansion of the failure surface due to the model's strain rate dependence is shown. The tensile failure surface is defined by

$$S_Y^{tens} = (C_1 - (C_2 + (C_1 - C_2)d)(1 + C_3 \ln(\dot{\varepsilon}_n))(T_{max} - I_1/)T_{max}, \tag{3}$$

where T_{max} is the maximum allowed tensile pressure, and the tensile failure surface evolves according to the same damage term as used for the compression surface. An important enhancement of the AFC model over similar constitutive models is inclusion of the third stress invariant for calculation of the extension failure surface. The extension failure surface is obtained by using the third stress invariant to calculate the Lode angle using a Willam–Warnke Lode function (Fossum and Brannon, 2006). A reduction factor is then computed that is multiplied by Eq. (2) to obtain the extension failure surface (Adley et al., 2010). A final constant in the failure surface definition is C_5, which is the maximum allowable principal stress on the failure surface.

The damage portion of the AFC model will now be discussed. In the original AFC model by Adley et al. (2010), evolution of the compression and tensile failure surfaces occurs according to the single damage parameter, d. As a consequence the original AFC model tensile behavior has a sharp discontinuity that is not desirable for numerical simulations that are driven by the tensile response (i.e., finite thickness slab perforation). Although typical, use of this single damage parameter does not account for the different failure mechanisms that occur during tensile and compression failure in the continuum. Therefore, a bi-scalar damage description was proposed for the AFC model (Chen et al., 2011; Roth et al., 2011) that is based on a multiscale two-parameter damage model (Ren et al., 2011). In the AFC bi-scalar damage description, separate damage evolution terms are defined for compression and tension. The compression damage, d_c, evolves according to

$$d_c = \sum[\Delta\varepsilon_p/(-I_1 D_1) + \Delta\mu_p/(1.5C_9)], \tag{4}$$

which is the evolution function described by the original AFC damage evolution algorithm. In Eq. (4), D_1 and C_9 are material constants, and $\Delta\varepsilon_p$ and $\Delta\mu_p$ are the plastic strain increment and volumetric strain increment, respectively. The damage value is allowed to increase only to a value of 1.0.

Tensile damage evolution in the AFC bi-scalar damage description is defined by a microcrack-informed damage model (MIDM) proposed by Ren et al. (2011). The MIDM was proposed to improve the description of softening behavior of brittle solids by replacing the continuum-scale phenomenological description of tensile damage with a damage evolution function that is derived from a model of fracture in the concrete microstructure. A representative microcell is used to describe the material microstructure, and brittle failure is explicitly modeled in the concrete substructure according to the fundamental laws of fracture mechanics. To provide the linkage to the continuum scale, the averaged microcell stress and strain are homogenized to the continuum, and equivalence is established between the Helmholtz free energy (HFE) of the cracked microcell and the HFE of the continuum (Ren et al., 2011). Conventional damage mechanics is then used to obtain a

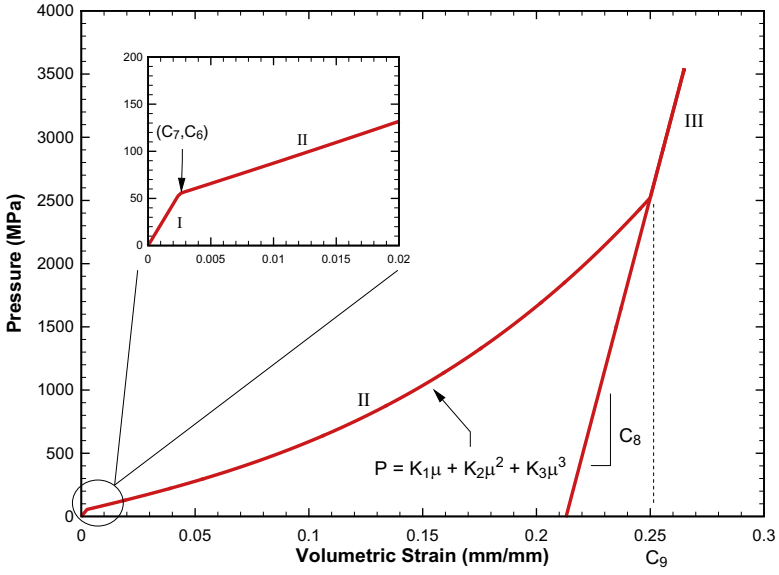

Fig. 1. The AFC hydrostatic fit for WES5000 concrete used in this study.

damage evolution function by relating the HFE of the cracked microcell, the HFE of the continuum, and the microcell homogenized stress and strain (Ren et al., 2011). The physical significance of this approach is that the purely phenomenological description of continuum-scale tensile failure is replaced with a new damage evolution function that is derived from the model of fine-scale fracture and failure at the microscale. Through this linkage between microstructure failure and continuum-scale damage, the MIDM approach not only improves on the damage description for material/system analysis but also provides a framework to assess the effects of microstructure modifications in the context of material design.

To determine the microcrack-informed tensile damage evolution function in this work, the microcell analysis was based on Mode I crack propagation in a center-cracked cell using a cohesive crack model (Roth et al., 2011). Solving the microcell boundary value problem and employing the MIDM energy bridging, the tensile damage vs. homogenized tensile strain relationship was determined (Roth et al., 2011), as shown in Fig. 3. The tensile damage parameter is referred to as d_t. This nonlinear damage evolution function was implemented to define tensile damage evolution in the AFC model. The AFC model with the multiscale two-parameter damage description is referred to as the MIDM-enhanced AFC model. The failure surface definitions in the MIDM-enhanced AFC model are

$$S_Y^{comp} = (C_1 - (C_2 + (C_1 - C_2)d_c)e^{A_n I_1} - C_4 I_1)(1 + C_3 \ln(\dot{\varepsilon}_n)), \tag{5}$$

$$S_Y^{tens} = (C_1 - (C_2 + (C_1 - C_2)d_c)(1 + C_3 \ln(\dot{\varepsilon}_n))\frac{T_{max}(1 - d_t) - I_1}{T_{max}(1 - d_t)}, \tag{6}$$

where the tensile failure surface is modified to incorporate the microcrack-informed tensile damage parameter. The overall result

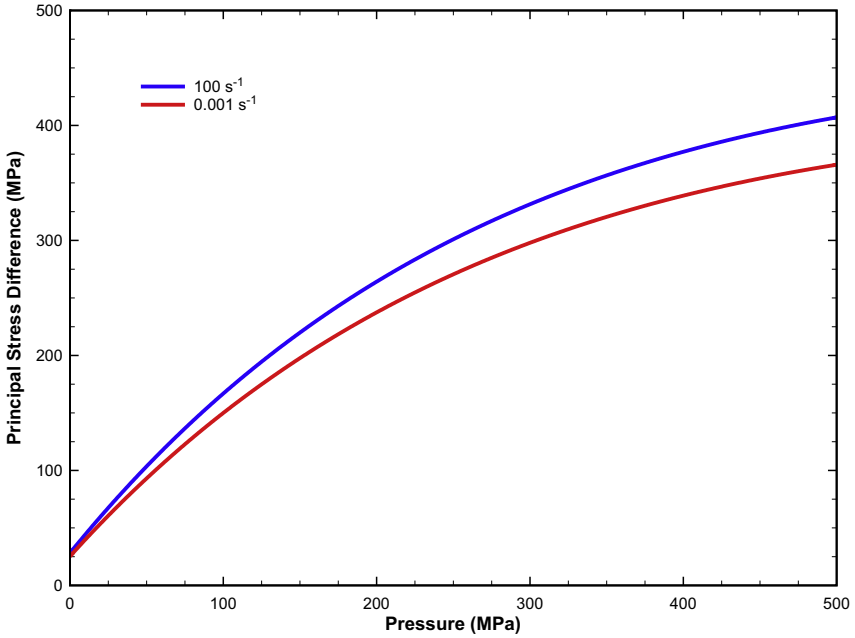

Fig. 2. AFC failure surface for WES5000 used in this study. Two different strain rates are shown in order to show the variation in strain rate response of the failure surface.

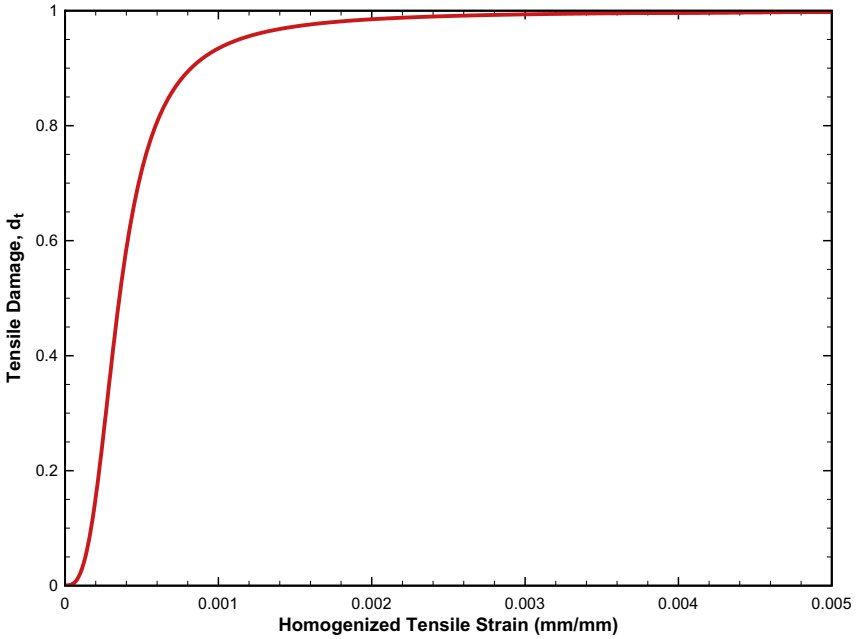

Fig. 3. Microcrack-informed tensile damage evolution function used for WES5000 in this study.

is a general framework that can define the tensile damage evolution better than the original implementation of the AFC model. Fig. 4 shows a comparison of the MIDM-enhanced AFC model tensile behavior compared to the AFC model compression behavior. The AFC material model constants are listed in Table 1.

One of the main difficulties of numerically modeling cementitious materials is the inherent stochastic nature of the material. A simplified approach was used to capture some of the inherent variations in the material. Two of the constants, C_1 and T_{max}, were chosen to represent the variation in the WES5000 concrete. C_1 was chosen because it directly affects the failure surface and it allows some control over the unconfined compressive strength. A small amount, 2.5%, of random variation was allowed over the whole concrete domain for C_1. The second constant, T_{max}, represents the maximum tensile pressure that the concrete can handle. A moderate variation, 10%, of this constant was also randomly varied over the concrete domain. Both of the constants were randomly varied over their respective ranges and were distributed over the concrete domain.

For modeling the 4340 steel casing in this study an elastic-perfectly plastic model was used. This choice is justified due to the minimal deformation that the penetrator experiences during the event. The yield stress of the material was set to 1500 MPa, and material density was 7850 kg/m^3. The inert (sand) filler material

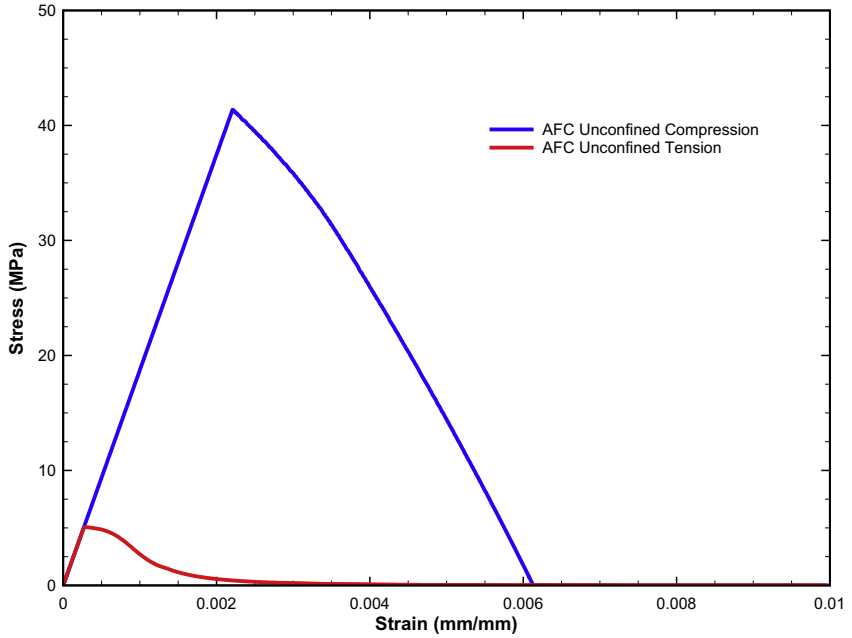

Fig. 4. A comparison of the MIDM-enhanced AFC unconfined tension response and unconfined compression response used in this study.

Table 1
AFC model constants for WES5000 used in this study.

Parameter	Value
Density (kg/m^3)	2267
Shear modulus (MPa)	6892.7
C_1 (MPa) – failure surface constant	501.05 ± 2.5%
C_2 (MPa) – failure surface constant	476.3
C_3 – failure surface constant	0.01
C_4 – failure surface constant	0.1
C_5 (MPa) – failure surface constant	516.95
C_6 (MPa) – pressure where crushing begins	55.14
C_7 – volumetric strain at crushing	0.0025
C_8 (MPa) – locking bulk modulus	68237
C_9 – volumetric strain at locking	0.25
K_1 (MPa) – hydrostatic compression constant	4248.3
K_2 (MPa) – hydrostatic compression constant	6196.5
K_3 (MPa) – hydrostatic compression constant	68237
D_1 (MPa^{-1}) – damage constant	0.0006
A_N (MPa^{-1}) – failure surface constant	0.00324
TXETXCR – third invariant ratio constant	0.625
T_{max} (MPa) – maximum allowable tensile pressure	2.47 ± 10%

was modeled using a Drucker Prager material model with a density of 1580 kg/m^3. The angle of friction and dilatation angle were assumed to be 30° and 5°, respectively.

3. Experimental setup

Cargile (1999) conducted experiments on cylindrical unreinforced concrete (WES5000) slabs with a nominal unconfined compressive strength of 38.2 MPa. The WES5000 concrete was characterized by a suite of laboratory materials characterization tests. The concrete slabs had a diameter of 1.52 m with thicknesses of 127 mm, 216 mm, or 257 mm.

The experiments used thin-walled, semi-armor piercing (SAP) projectiles, illustrated in Fig. 5, machined from 4340 steel and subsequently hardened to a Rockwell hardness of 43–45. The interior cavity of each projectile was filled with inert filler (sand); the total mass of the projectile and filler was 2.343 kg. The SAP projectiles were launched into the concrete targets at a velocity of approximately 313 m/s using an 83-mm-diameter solid-propellant gun. All impacts were normal to the surface of the target slab.

Perforation of the target was observed in each of the experiments. Observed impact craters were significantly smaller than exit craters with the size of the exit crater increasing with slab thickness. Cracks observed on the front of the targets were found to extend through the depth of the target. Images from high-speed movies of the impact indicated that a small amount of pulverized material and small pieces of concrete were ejected from the impact face of the target. Damage to the exit face of the target was observed to begin with radial cracking on the back face opposite the point of impact culminating with formation of an exit crater as material was pushed from the back face of the slab. The sizes of the pieces of concrete pushed from the exit face generally increased in size and decreased in number as slab thickness increased. The projectiles experienced little deformation during the perforation events because of the significant difference in strength between the SAP projectile and the concrete.

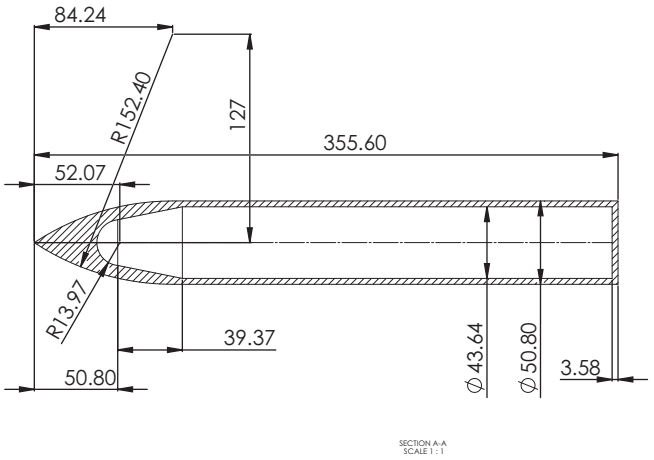

Fig. 5. Dimensions of SAP projectile used in Cargile (1999) and modeled in this study. All dimensions are in millimeters.

4. Numerical model setup

The simulation software Abaqus (Abaqus, 2012) was used in this study. Abaqus is a traditional finite element analysis package that has a CEL modeling feature. The CEL method in Abaqus has been shown to be an excellent method for problems involving a penetrator into concrete (Abaqus, 2009). The SAP perforation simulation model contained the SAP projectile and the WES5000 concrete targets with different thicknesses. Since the concrete target experiences large deformation during the penetration event, it was modeled as an Eulerian part. The size of the Eulerian domain needs to be large enough to accommodate the initial impact ejecta as well as the emerging debris field as the penetrator exits the concrete slab. Due to the symmetry of the experiment only half of the problem domain was modeled. A large enough Eulerian domain was created for the thickest slab, 254 mm, and the other two slab thicknesses, 127 and 216 mm, used the same domain size. The Eulerian domain consisted of 778,160 elements. The SAP penetrator was modeled with 5620 reduced order hexahedral elements

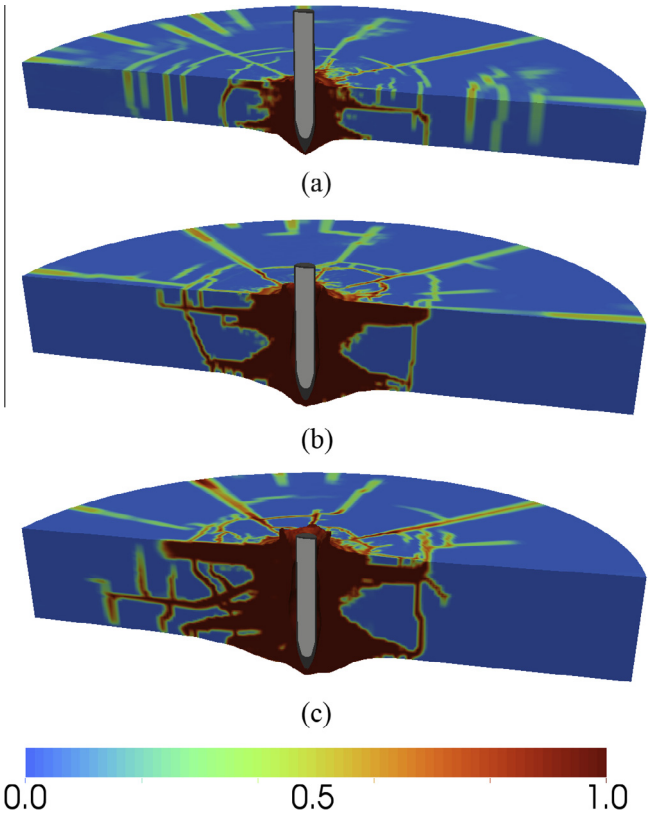

Fig. 6. Damage contours for SAP projectile perforation CEL models for thicknesses of (a) 127 mm, (b) 216 mm, and (c) 254 mm.

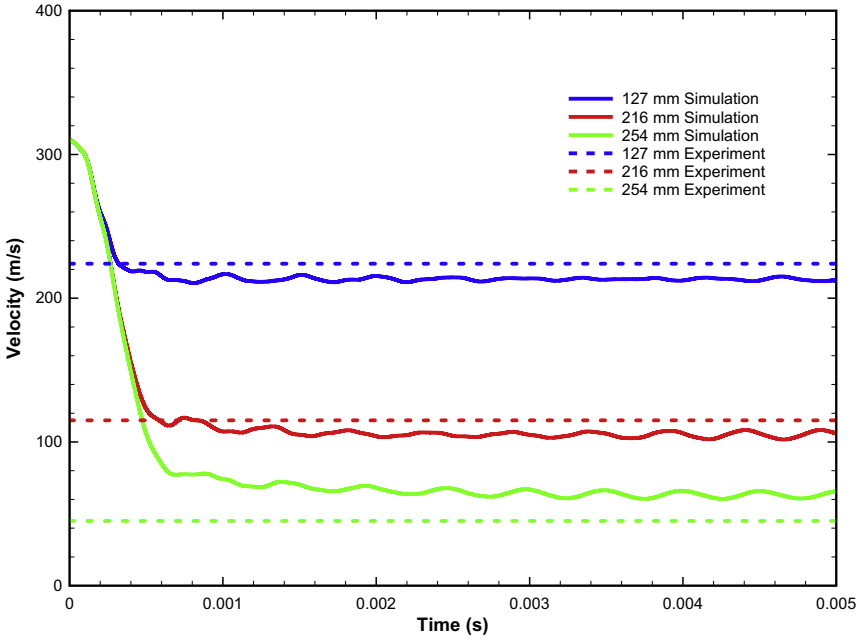

Fig. 7. Averaged velocity time history of the SAP penetrator for the three different slab thicknesses.

Table 2
Comparison between SAP projectile experiments and averaged Abaqus CEL simulations.

Thickness (mm)	Experimental exit velocity (m/s)	Experimental Δ velocity (%)	Experiment Δ KE (%)	Simulation exit velocity (m/s)	Simulation Δ velocity (%)	Simulation Δ KE (%)
127	224	28.4	48.8	212.5	32.1	53.9
216	115	63.3	86.5	104.9	66.5	88.8
254	45	85.6	97.9	63.2	79.8	95.9

which included both the 4340 steel casing and the inert fill. The initial velocity of the penetrator for each slab thickness was 313 m/s as described in Section 3. The contact between the Lagrangian penetrator and the Eulerian concrete slab is controlled by Abaqus' general contact algorithm. This Eulerian–Lagrangian general contact formulation is based on an enhanced immersed boundary method (Abaqus, 2012). The formulation automatically tracks the interface between the Lagrangian and Eulerian surfaces.

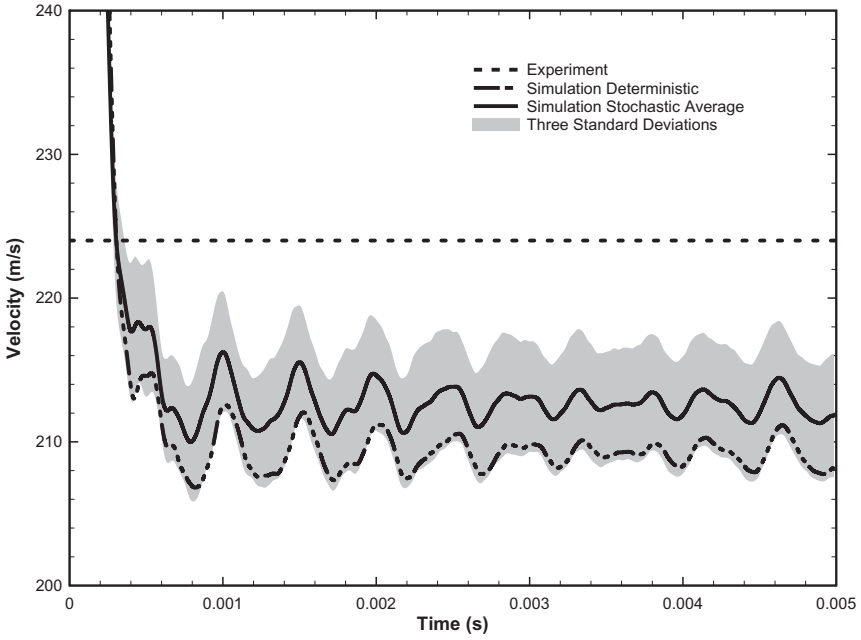

Fig. 8. Averaged velocity–time history for 127 mm slab thickness which includes three standard deviations of simulation variation and the velocity–time history for the deterministic simulation (note the zoomed in velocity scale).

The AFC material model was implemented as a user defined material in Abaqus that was originally implemented in Sherburn et al. (2011).

Due to the non-deterministic nature of these simulations introduced in the material by varying C_1 and T_{max}, each concrete slab thickness simulation was run 15 times to get an averaged response of the event. For comparison, a respective deterministic (constant C_1 and T_{max}) calculation was also run for each slab thickness. Each simulation ran until the SAP projectile exited the back of the slab, and then the simulation was stopped.

In order to show the strength of the CEL method in Abaqus, corresponding pure Lagrangian simulations were also run. These problems required erosion criteria for the elements in order to prevent mesh entanglement and model instability. The elements were eroded when the plastic strain reached a specified amount. Two different plastic strain criteria (1.5 and 2.25) were used to show the effects of the subjective plastic strain criteria on the Lagrangian simulations. These Lagrangian simulations were performed as deterministic simulations for comparison to the deterministic CEL simulations.

5. Results and discussion

A sampling of the stochastic simulation results for all three slab thicknesses is shown in Fig. 6 near the point when the projectile exits the target. One general trend is that with an increase in target thickness the model predicts a larger damaged volume. The larger damaged volume is due to the increased amount of energy absorbed by the target as the target thickness increases. The asymmetry of the damage patterns is partly produced by the random distribution of the C_1 and T_{max} constants, and some of the randomness was due to numerical effects. Even though the damage patterns were different every time the simulation was run, common patterns emerged in all the simulations. One common feature in the simulations was the presence of at least three radial cracks that developed from the impact location. As shown in Fig. 6 the SAP penetrator experienced little deformation during all three penetration simulations.

The simulations matched the experimental data reasonably well as shown in the velocity–time history data in Fig. 7. The velocity–time history data shown in Fig. 7 was averaged over all the 15 simulations that were performed for each slab thickness. A direct comparison between the averaged Abaqus results and the experimental data is shown in Table 2. The largest change in exit velocity difference between the experiment and simulations was 5.8% on the 254 mm target. However, when comparing change in kinetic energy between the experiment and simulations the 127 mm target had the largest percentage difference of 5.1%.

Due to the random distribution of C_1 and T_{max} the velocity–time history had some expected variation. Fig. 8 displays the average velocity–time history of the 127 mm slab including the variation of three standard deviations from the 15 simulations along with the deterministic simulation. The maximum standard deviation over the time frame was 1.65 m/s for this simulation series. The amount of variation induced by the random distribution of the constants provided little change to the overall velocity–time history profile. The difference between damage patterns of three different stochastic simulations of the 127 mm simulation and the deterministic simulation is highlighted in Fig. 9. Slightly different damage patterns emerged from the random variation of the concrete domain compared to the deterministic case, where the randomness was due to the inherent behavior of the numerical solution for a softening material. In some of the simulations, like Fig. 9b, the damage near the bottom surface would grow larger than the other side. The asymmetric deformation patterns induced a small amount of rotation in the SAP penetrator in all the simulations. The average angle produced by the slab at 2.25 ms was 1.55° with a corresponding average rotation rate of 767.2 degree/s. The random distribution of C_1 and T_{max} was chosen for this study as an initial step to investigate the heterogeneous nature of concrete under these extreme loading conditions. While the random distribution is not physically accurate, future studies will be carried out to determine which constants should be varied and the proper magnitude of variation. Future studies will also investigate realistic physical distributions of the material variation instead of the random distribution used in this study.

The purely Lagrangian calculations compared to the CEL method showed the greatest amount of difference for the 254 mm thickness slab. Fig. 10 shows the results of the 254 mm deterministic simulations for the CEL method, the Lagrangian simulation with plastic strain erosion criteria of 1.5 and 2.25, and the experimental data. Higher values of erosion criteria were evaluated during this study, but anything higher than 2.25 resulted in excessive amounts of slab resistance in the 127 and 216 mm cases compared to the experiments. One of the key differences in the Lagrangian analysis compared to the CEL analysis is that it requires the erosion criteria to remain stable. The erosion criterion is subjective and does not have physical meaning for concrete. Furthermore, the variation of the erosion criteria can significantly affect the results. The CEL method has an advantage over the

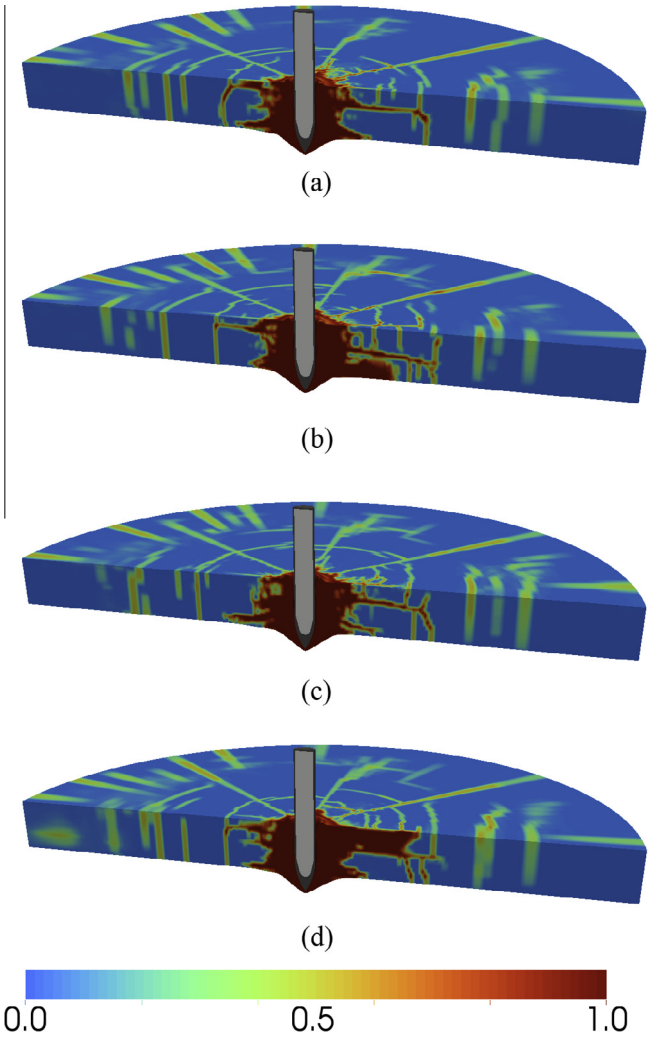

Fig. 9. The damage distribution from three different stochastic simulation results due to the random variation of the concrete material (a–c). The results of the deterministic simulation (d) is also included for comparison.

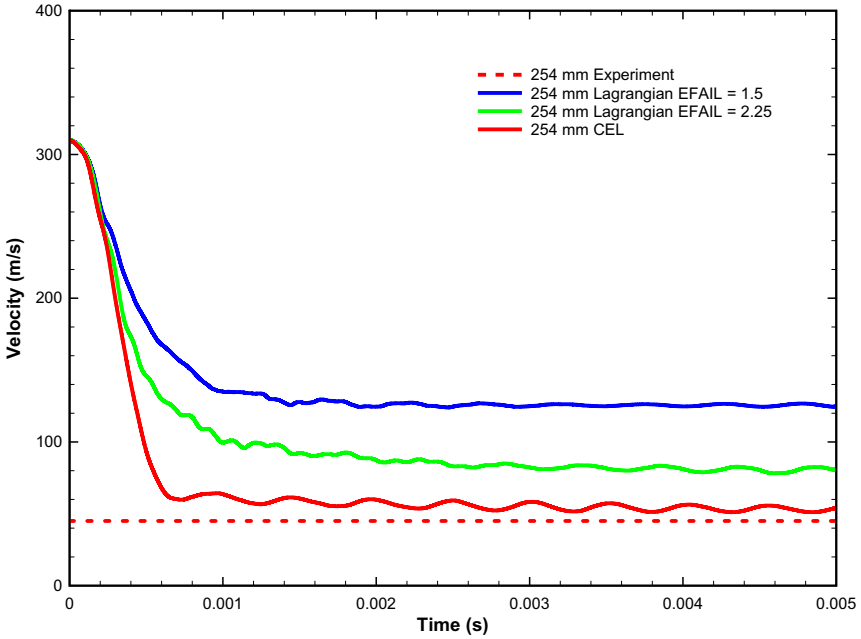

Fig. 10. Comparison of CEL method to Lagrangian method with erosion for the 254 mm slab. All simulation results were for the deterministic cases.

purely Lagrangian method by not requiring the additional subjective erosion criteria.

6. Conclusions

In this study a CEL approach in Abaqus was used to model the perforation of a SAP projectile into finite thicknesses concrete slabs. The implementation of the AFC model described in this work as a user defined material in Abaqus enabled reasonable results matching experimental data. The addition of a random distribution of material constants produced a variation of damage patterns that are also present in the experimental results; however, more future work will be required in this area. The overall results of the simulations performed in this study show that the CEL approach in Abaqus is an excellent method to model the perforation of finite thickness concrete slabs by a nearly rigid penetrator.

Acknowledgments

Permission to publish was granted by the Director, Geotechnical and Structures Laboratory. Simulations were performed on the Department of Defense Super Computing Resource high performance computers.

References

Abaqus®/Explicit User Manual, Version 6.12, Simulia®, 2012.
Abaqus® Technology Brief. 2009. Earth Penetrating Simulation using Coupled Eulerian–Lagrangian Analysis. Simulia, TB-09-PEN-1.
Adley, M.D., Frank, A.O., Danielson, K.T., Akers, S.A, O'Daniel, J.L., 2010. The advanced fundamental concrete (AFC) model, Technical Report ERDC/GSL TR-10-51, Vicksburg, MS: U.S. Army Engineer Research and Development Center.
Anderson, C.E., 1987. An overview of hydrocodes. Int. J. Impact Eng. 5 (4), 33–55.
Aptukov, V.N., 1990. Penetration: mechanical aspects and mathematical modeling (Review). Strength Mater. 22 (2), 230–240.
Backman, M.E., Goldsmith, W., 1978. The mechanics of penetration of projectiles into targets. Int. J. Eng. Sci. 16, 1–99.
Belytschko, T., Lin, A., 1987. A three-dimensional impact-penetration algorithm with erosion 1987. Int. J. Impact. Eng. 5, 111–127.
Ben-Dor, G., Dubinsky, A., Elperin, T., 2005. Recent advances in analytical modeling of plate penetration dynamics – a review. Appl. Mech. Rev. 58, 355–371.
Benson, D.J., 1992. Computational methods in Lagrangian and Eulerian hydrocodes. Comput. Methods Appl. Mech. Eng. 99, 235–394.
Brown, K.H., Burns, S.P., Christon, M.A., 2002. Coupled Eulerian–Lagrangian methods for earth penetrating weapon applications, SAND2002-1014, Sandia National Laboratories.
Cargile, J.D., 1999. Development of a constitutive model for numerical simulation of projectile penetration into brittle geomaterials, Technical Report SL-99-11, US Army Corps of Engineers Engineer Research and Development Center.
Chen, J.S., Pan, C.H., Wu, C.T., Yoon, S., Liu, W.K., 1996. Reproducing kernel particle methods for large deformation analysis of non-linear structures. Comput. Methods Appl. Mech. Eng. 139, 195–227.
Chen, J.S., Chi, S.W., Lee, C.H., Lin, S.P., Marodon, C. Roth, M.J., Slawson, T.R., 2011. A multiscale meshfree approach for modeling fragment penetration into ultra high-strength concrete, Technical Report ERDC/GSL TR-11-35, US Army Corps of Engineers Engineer Research and Development Center.
Forrestal, M.J., Luk, V.K., 1992. Penetration into soil targets. Int. J. Impact Eng. 12 (3), 427–442.
Forrestal, M.J., Altman, B.K., Cargile, J.D., Hanchak, S.J., 1994. An empirical equation for penetration depth of ogive-nose projectiles into concrete targets. Int. J. Impact Eng. 15 (4), 395–405.
Guan, P.C., Chi, S.W., Chen, J.S., Slawson, T.R., Roth, M.J., 2011. Semi-Lagrangian reproducing kernel particle method for fragment-impact problems. Int. J. Impact Eng. 38, 1033–1047.
Holmquist, T.J., Johnson, G.R., Cook, W.H., 1993. A computational constitutive model for concrete subjected to large strains, high strain rates, and high pressures. In: 14th International Symposium of Ballistics, Quebec, Canada, pp. 591–600.
Fossum, A.F., Brannon, R.M., 2006. On a viscoplastic model for rocks with mechanism-dependent characteristic times. Acta Geotech. 1, 89–106.
Johnson, G.R., Stryk, R.A., 1987. Eroding interface and improved tetrahedral element algorithms for high-velocity impact computations in three dimensions. Int. J. Impact Eng. 5, 411–421.
Johnson, G.R., Stryk, R.A., Beissel, S.R., 1996. SPH for high velocity impact computation. Comput. Methods Appl. Mech. Eng. 139, 343–373.
Johnson, G.R., Stryk, R.A., Beissel, S.R., 2000. A generalized particle algorithm for high velocity impact computations. Comput. Mech. 25, 245–256.
Jonas, G.H., Zukas, J.A., 1978. Mechanics of penetration: analysis and experiment. Int. J. Eng. Sci. 16, 879–903.
Kennedy, R.P., 1976. A review of procedures for the analysis and design of concrete structures to resist missile impact effects. Nucl. Eng. Des. 37, 183–203.
Ren, X., Chen, J.S., Li, J., Slawson, T.R., Roth, M.J., 2011. Micro-cracks informed damage models for brittle solids. Int. J. Solids Struct. 48, 1560–1571.
Roth, M.J., Chen, J.S., Slawson, T.R., Boone, R.N., Ren, X., Chi, S.W., Lee, C.H., Guan, P.C., 2011. Multiscale RKPM formulation for modeling penetration of an ultra high-strength concrete material. In: Proceedings of Computational Methods in Structural Dynamics and Earthquake Engineering, Corfu, Greece, May 26–28.
Sewell, D.A., Ong, A.C.J., Hallquist, J.O., 1990. Penetration calculation using an erosion algorithm in DYNA. In: Proceedings of the 12th International Symposium on Ballistics, vol. 3, San Antonio, pp. 208–217.
Sherburn, J.A., Heard, W.F., Park, H., Chen, W., 2011. Modeling of the split Hopkinson pressure bar: application to Cortuf. In: Presented at 82nd SAVIAC, Baltimore, MD, October 30–November 4.
White, M.P., 1946. Effects of impact and explosion. Office of Scientific Research and Development, Washington, DC.
Wilkins, M.L., 1978. Mechanics of penetration and perforation. Int. J. Eng. Sci. 16, 793–807.